Bryant, J. J., Bland-Hawthorn, J., Lawrence, J., et al. 2020, in Society of Photo-Optical Instrumentation Engineers (SPIE) Conference Series, Vol. 11447, Society of Photo-Optical Instrumentation Engineers (SPIE) Conference Series, 1144715

Bundy, K., Bershady, M. A., Law, D. R., et al. 2015, The Astrophysical Journal, 798, doi:10.1088/0004-637X/798/1/7

Camps, P., & Baes, M. 2020, Astronomy and Computing, 31, 100381

Cappellari, M. 2002, Monthly Notices of the Royal Astronomical Society, 333, 400

Cappellari, M. 2017, Monthly Notices of the Royal Astronomical Society, 466, 798

Cappellari, M., & Emsellem, E. 2004, Publications of the Astronomical Society of the Pacific, 116, 138

Cappellari, M., Emsellem, E., Bacon, R., et al. 2007, Monthly Notices of the Royal Astronomical Society, 379, 418

Cappellari, M., Emsellem, E., Krajnović, D., et al. 2011, Monthly Notices of the Royal Astronomical Society, 413, 813

Chabrier, G. 2003, The Publications of the Astronomical Society of the Pacific, 115, 763

Crain, R. A., Schaye, J., Bower, R. G., et al. 2015, Monthly Notices of the Royal Astronomical Society, 450, 1937

Croom, S. M., Lawrence, J. S., Bland-Hawthorn, J., et al. 2012, Monthly Notices of the Royal Astronomical Society, 421, 872

Croom, S. M., Taranu, D. S., van de Sande, J., et al. 2021, Monthly Notices of the Royal Astronomical Society, 505, 2247

de Zeeuw, P. T., Bureau, M., Emsellem, E., et al. 2002, Monthly Notices of the Royal Astronomical Society, 329, 513

Doi, M., Tanaka, M., Fukugita, M., et al. 2010, AJ, 139, 1628

Dolag, K., Hansen, F. K., Roncarelli, M., & Moscardini, L. 2005, Monthly Notices of the Royal Astronomical Society, 363, 29

Dubois, Y., Pichon, C., Welker, C., et al. 2014, Monthly Notices of the Royal Astronomical Society, 444, 1453

Emsellem, E., Cappellari, M., Peletier, R. F., et al. 2004, Monthly Notices of the Royal Astronomical Society, 352, 721

Fletcher, R. 1970, The Computer Journal, 13, 317

Forsythe, Malcolm, M. A., & Moler, M. A. and. 1977, Computer Methods for Mathematical Computations (Wiley)

Foster, C., Mendel, J. T., Lagos, C. D. P., et al. 2021, PASA, 38, e031

Fukugita, M., Ichikawa, T., Gunn, J. E., et al. 1996, AJ, 111, 1748

Goldfarb, D. 1970, Mathematics of Computation, 24, 23

Harborne, K. E., Power, C., & Robotham, A. S. G. 2020a, Publications of the Astronomical Society of Australia, 37, doi:10.1017/pasa.2020.8

Harborne, K. E., Power, C., Robotham, A. S. G., Cortese, L., & Taranu, D. S. 2019, Monthly Notices of the Royal Astronomical Society, 483, 249

Harborne, K. E., van de Sande, J., Cortese, L., et al. 2020b, Monthly Notices of the Royal Astronomical Society, 497, 2018

Hogg, D. W. 1999, arXiv e-prints, astro

Jesseit, R., Cappellari, M., Naab, T., Emsellem, E., & Burkert, A. 2009, Monthly Notices of the Royal Astronomical Society, 397, 1202

Jesseit, R., Naab, T., Peletier, R. F., & Burkert, A. 2007, Monthly Notices of the Royal Astronomical Society, 376, 997

Jiménez, E., Lagos, C. d. P., Ludlow, A. D., & Wisnioski, E. 2023, Monthly Notices of the Royal Astronomical Society, 524, 4346

Katz, N., Weinberg, D. H., & Hernquist, L. 1996, The Astrophysical Journal Supplement Series, 105, 19

Lagos, C. d. P., Emsellem, E., van de Sande, J., et al. 2022, Monthly Notices of the Royal Astronomical Society, 509, 4372

Li, H., Mao, S., Emsellem, E., et al. 2018, Monthly Notices of the Royal Astronomical Society, 473, 1489

Ludlow, A. D., Fall, S. M., Wilkinson, M. J., Schaye, J., & Obreschkow, D. 2023, arXiv e-prints, arXiv:2306.05753

Ludlow, A. D., Schaye, J., Bower, R., et al. 2019, Monthly Notices of the Royal Astronomical Society, 488, 3663

Metzler, C. A., & Evrard, A. E. 1994, The Astrophysical Journal, 437, 564

Moffat, A. F. J. 1969, Astronomy and Astrophysics, 3, 455

Naab, T., Oser, L., Emsellem, E., et al. 2014, Monthly Notices of the Royal Astronomical Society, 444, 3357

Nanni, L., Thomas, D., Trayford, J., et al. 2022, Monthly Notices of the Royal Astronomical Society, 515, 320

Nanni, L., Thomas, D., Trayford, J., et al. 2023, Monthly Notices of the Royal Astronomical Society, 522, 5479

Nelson, D., Pillepich, A., Springel, V., et al. 2019, Monthly Notices of the Royal Astronomical Society, 490, 3234

Nelson, D., Pillepich, A., Springel, V., et al. 2019, Monthly Notices of the Royal Astronomical Society, 490, 3234

Oser, L., Ostriker, J. P., Naab, T., Johansson, P. H., & Burkert, A. 2010, The Astrophysical Journal, 725, 2312

Pillepich, A., Springel, V., Nelson, D., et al. 2018, Monthly Notices of the Royal Astronomical Society, 473, 4077

Pillepich, A., Nelson, D., Springel, V., et al. 2019, Monthly Notices of the Royal Astronomical Society, 490, 3196

Poci, A., McDermid, R. M., Lyubenova, M., et al. 2021, Astronomy & Astrophysics, 647, A145

Price, D. J. 2007, PASA, 24, 159

Robotham, A. S. G., Bellstedt, S., Lagos, C. d. P., et al. 2020, ProSpect: Generating Rapid Spectral Energy Distributions with Complex Star Formation and Metallicity Histories

Robotham, A. S. G., Taranu, D. S., Tobar, R., Moffett, A., & Driver, S. P. 2017, Monthly Notices of the Royal Astronomical Society, 466, 1513

Sarmiento, R., Huertas-Company, M., Knapen, J. H., et al. 2023, Astronomy & Astrophysics, 673, A23

Schaller, M., Dalla Vecchia, C., Schaye, J., et al. 2015, Monthly Notices of the Royal Astronomical Society, 454, 2277

Schaye, J., Crain, R. A., Bower, R. G., et al. 2015, Monthly Notices of the Royal Astronomical Society, 446, 521

Schulze, F., Remus, R. S., Dolag, K., et al. 2018, Monthly Notices of the Royal Astronomical Society, 480, 4636

Shanno, D. F. 1970, Math. Comp., 24, 647

Springel, V. 2005, Monthly Notices of the Royal Astronomical Society, 364, 1105

Springel, V., Pakmor, R., Pillepich, A., et al. 2018, Monthly Notices of the Royal Astronomical Society, Volume 475, Issue 1, p.676-698, 475, 676

Teklu, A. F., Remus, R. S., Dolag, K., et al. 2015, The Astrophysical Journal, 812, 29

van de Sande, J., Lagos, C. D., Welker, C., et al. 2019, Monthly Notices of the Royal Astronomical Society, 484, 869

van der Marel, R. P., & Franx, M. 1993, The Astrophysical Journal, 407, 525

Vazdekis, A., Koleva, M., Ricciardelli, E., Röck, B., & Falcón-Barroso, J. 2016, Monthly Notices of the Royal Astronomical Society, 463, 3409

Wendland, H. 1995, Advances in Computational Mathematics, 4, 389

Wilkinson, M. J., Ludlow, A. D., Lagos, C. d. P., et al. 2023, Monthly Notices of the Royal Astronomical Society, 519, 5942

Yurin, D., & Springel, V. 2014, Monthly Notices of the Royal Astronomical Society, 444, 62

Zhu, L., Pillepich, A., van de Ven, G., et al. 2022, Astronomy & Astrophysics, 660, A20

Appendix 1. Additional case study figures -

Appendix 1.1 Observations of intrinsic template spectral resolution at low redshift

Here, in Figures 16-20, we present the young bulge and old bulge observations from case study 1, where we have used the intrinsic spectral resolution of the underlying templates at a negligible redshift of $z = 0.0144$. The hexagonal maps are those models that have been built with the BC03 templates, while the circular maps have been built with the E-MILES templates. We can see a proportion of the pixels fit in the bulge E-MILES maps return an extremely low value of the observed dispersion (with equally extreme h_4 values), which may be reduced by increasing the signal-to-noise of the image as shown in the following Figures 16 and 17, either at the SimSpin construction stage, or through binning techniques not explored here.

Appendix 1.2 Observations of intrinsic template spectral resolution at high redshift

Here, in Figures 21-24, we present the young disc and old bulge observations from case study 2, where we have used the intrinsic spectral resolution of the underlying templates shifted up to a redshift of $z = 0.3$. The hexagonal maps are those models that have been built with the BC03 templates, while the circular maps have been built with the E-MILES templates.

Appendix 1.3 Observations of with `telescope()` spectral resolution at low & high redshift

Here, in Figures 25-26, we present the young disc low-z observations from case study 3, where we have used `telescope()` spectral resolutions of 3.61Å and 4.56Å for the E-MILES and BC03 models respectively. The hexagonal maps are those models that have been built with the BC03 templates, while the circular maps have been built with the E-MILES templates.

Appendix 1.4 Observations of with `telescope()` spectral resolution with atmospheric seeing conditions included.

Here, in Figures 27-28, we present the young disc high-z observations for the E-MILES model and low-z observations for the BC03 model from case study 4, where we have used `telescope()` spectral resolutions of 3.61Å and 4.56Å for the E-MILES and BC03 models respectively, and added different levels of seeing conditions by convolving each spatial plane with a convolution kernel. The hexagonal maps are those models that have been built with the BC03 templates, while the circular maps have been built with the E-MILES templates.

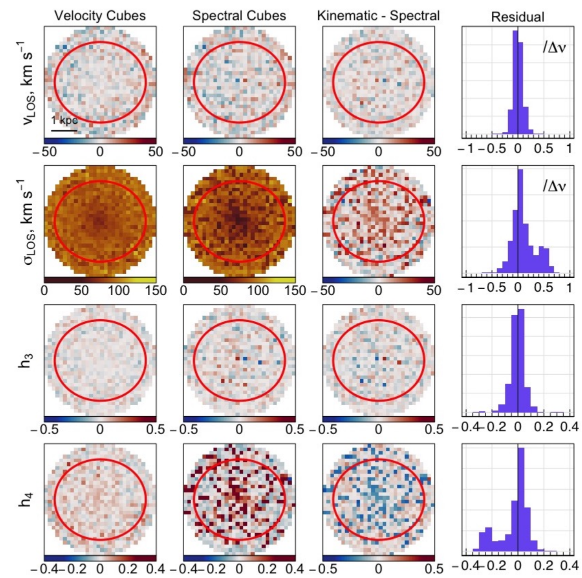

Figure 16. Case Study 1: The bulge model built with E-MILES templates observed with an intrinsic telescope resolution of $\lambda_{\rm LSF}^{telescope} = 0$ Å at a low redshift distance of $z = 0.0144$ with median signal-to-noise of 30. Here we compare the output kinematic cubes to the kinematics fit with pPXF, where the average spaxel fit $\chi^2/DOF = 1.03$.

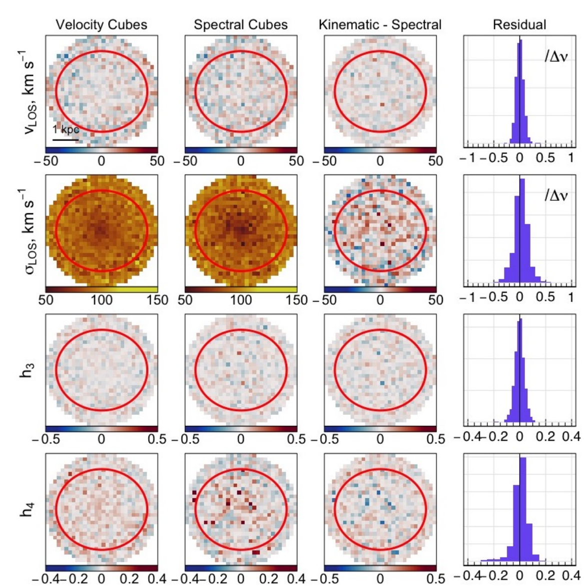

Figure 17. Case Study 1: The bulge model built with E-MILES templates observed with an intrinsic telescope resolution of $\lambda_{\rm LSF}^{telescope} = 0$ Å at a low redshift distance of $z = 0.0144$ with *minimum* signal-to-noise of 30. Here we compare the output kinematic cubes to the kinematics fit with pPXF and find a smoother recovery of the underlying dispersion, where the average spaxel fit $\chi^2/DOF = 1.13$.

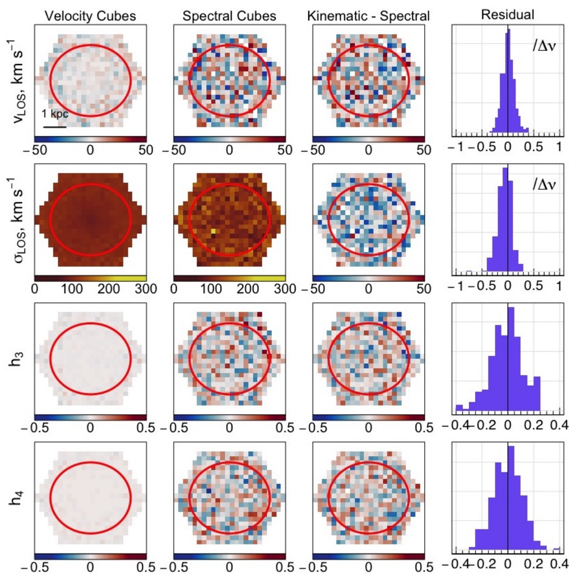

Figure 18. Case Study 1: The bulge model built with BC03 templates observed with an intrinsic telescope resolution of $\lambda_{\text{LSF}}^{telescope} = 0$ Å at a low redshift distance of $z = 0.0144$. Here we compare the output kinematic cubes to the kinematics fit with pPXF, where the average spaxel fit $\chi^2/DOF = 4.08$.

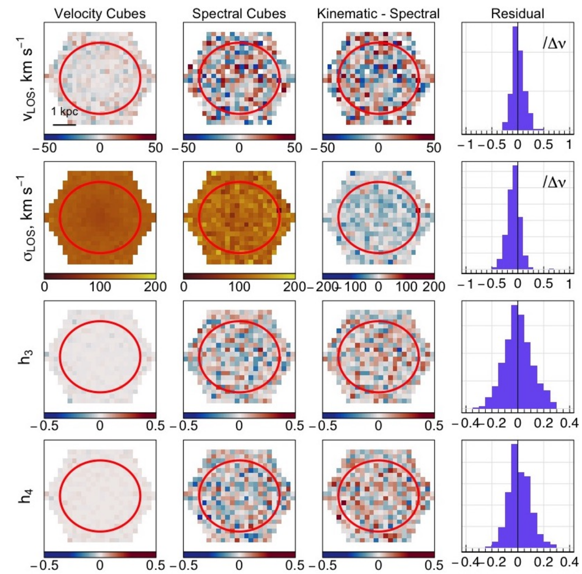

Figure 20. Case Study 1: The old bulge model built with BC03 templates observed with an intrinsic telescope resolution of $\lambda_{\text{LSF}}^{telescope} = 0$ Å at a low redshift distance of $z = 0.0144$. Here we compare the output kinematic cubes to the kinematics fit with pPXF, where the average spaxel fit $\chi^2/DOF = 3.64$.

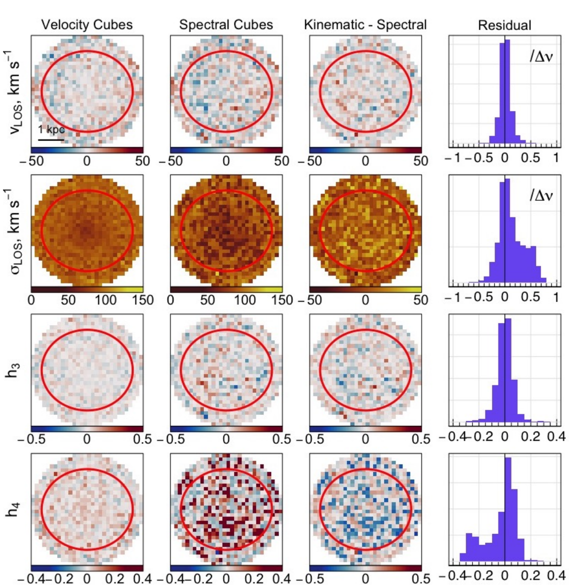

Figure 19. Case Study 1: The old bulge model built with E-MILES templates observed with an intrinsic telescope resolution of $\lambda_{\text{LSF}}^{telescope} = 0$ Å at a low redshift distance of $z = 0.0144$ and minimum signal-to-noise of 30. Here we compare the output kinematic cubes to the kinematics fit with pPXF, where the average spaxel fit $\chi^2/DOF = 0.99$.

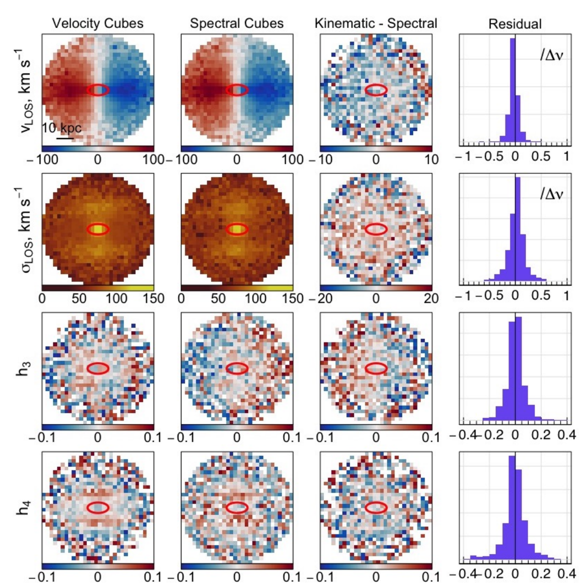

Figure 21. Case Study 2: The disk model built with E-MILES templates observed with an intrinsic telescope resolution of $\lambda_{\text{LSF}}^{telescope} = 0$ Å at a high redshift distance of $z = 0.3$. Here we compare the output kinematic cubes to the kinematics fit with pPXF, where the average pixel fit $\chi^2/DOF = 0.97$. The final column shows histogram of the relative residuals between the "velocity" and "spectral" kinematic maps, with the v_{LOS} and σ_{LOS} given with respect to the velocity resolution of the telescope.

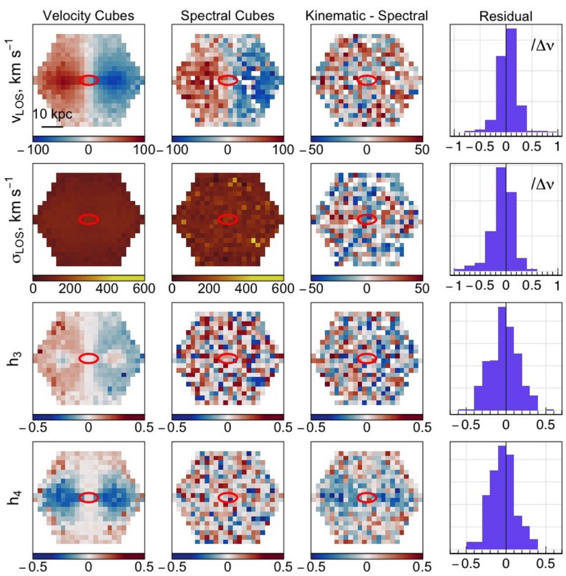

Figure 22. Case Study 2: The disk model built with BC03 templates observed with an intrinsic telescope resolution of $\lambda^{telescope}_{\mathrm{LSF}} = 0$ Å at a high redshift distance of $z = 0.3$. Here we compare the output kinematic cubes to the kinematics fit with pPXF, where the average pixel fit $\chi^2/DOF = 71.66$. The final column shows histogram of the relative residuals between the "velocity" and "spectral" kinematic maps, with the v_{LOS} and σ_{LOS} given with respect to the velocity resolution of the telescope.

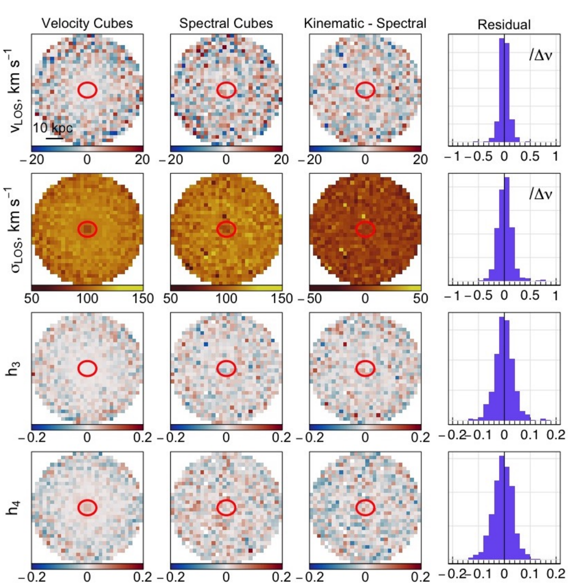

Figure 23. Case Study 2: The old bulge model built with E-MILES templates observed with an intrinsic telescope resolution of $\lambda^{telescope}_{\mathrm{LSF}} = 0$ Å at a high redshift distance of $z = 0.3$. Here we compare the output kinematic cubes to the kinematics fit with pPXF, where the average pixel fit $\chi^2/DOF = 1.05$. The final column shows histogram of the relative residuals between the "velocity" and "spectral" kinematic maps, with the v_{LOS} and σ_{LOS} given with respect to the velocity resolution of the telescope.

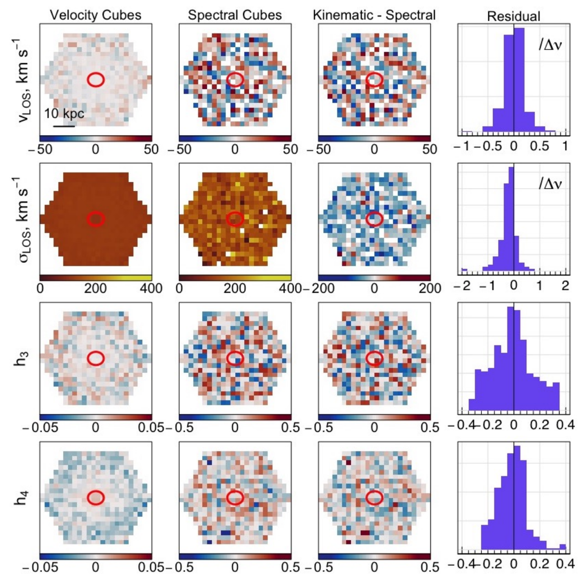

Figure 24. Case Study 2: The old bulge model built with BC03 templates observed with an intrinsic telescope resolution of $\lambda^{telescope}_{\mathrm{LSF}} = 0$ Å at a high redshift distance of $z = 0.3$. Here we compare the output kinematic cubes to the kinematics fit with pPXF, where the average pixel fit $\chi^2/DOF = 37.66$. The final column shows histogram of the relative residuals between the "velocity" and "spectral" kinematic maps, with the v_{LOS} and σ_{LOS} given with respect to the velocity resolution of the telescope.

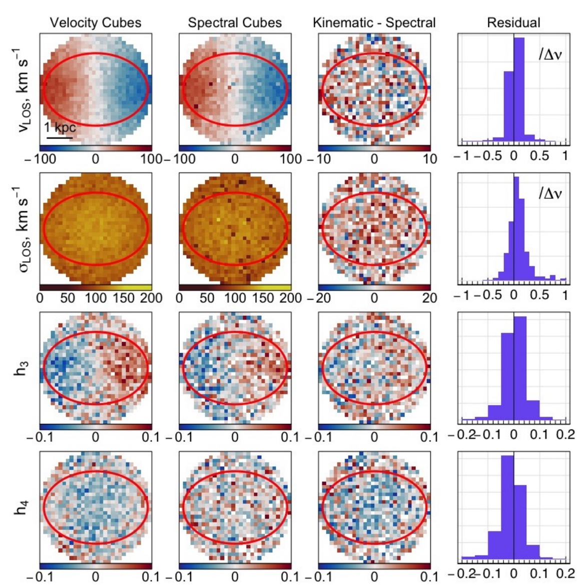

Figure 25. Case Study 3: The disk model built with E-MILES templates observed with an intrinsic telescope resolution of $\lambda^{telescope}_{\mathrm{LSF}} = 3.61$ Å at a low redshift distance of $z = 0.0144$. Here we compare the output kinematic cubes to the kinematics fit with pPXF, where the average pixel fit $\chi^2/DOF = 2.02$. The final column shows histogram of the relative residuals between the "velocity" and "spectral" kinematic maps, with the v_{LOS} and σ_{LOS} given with respect to the velocity resolution of the telescope.

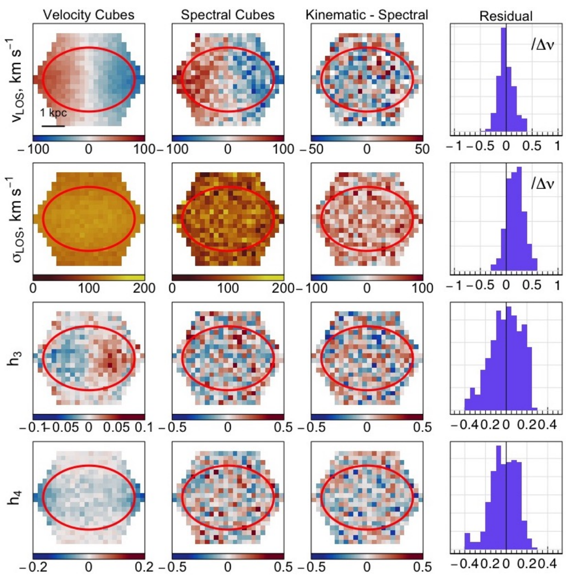

Figure 26. Case Study 3: The disk model built with BC03 templates observed with an intrinsic telescope resolution of $\lambda_{\rm LSF}^{telescope}$ = 4.56 Å at a low redshift distance of z = 0.0144. Here we compare the output kinematic cubes to the kinematics fit with pPXF, where the average pixel fit χ^2/DOF = 5.05. The final column shows histogram of the relative residuals between the “velocity” and “spectral” kinematic maps, with the v_{LOS} and σ_{LOS} given with respect to the velocity resolution of the telescope.

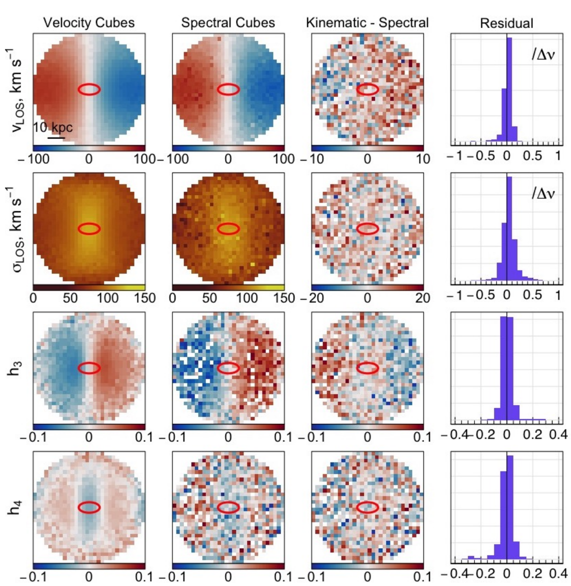

Figure 27. Case Study 4: The disk model built with E-MILES templates observed with an intrinsic telescope resolution of $\lambda_{\rm LSF}^{telescope}$ = 3.61 Å at a high redshift distance of z = 0.3. We convolve each plane in this cube with a Moffat kernel with FWHM of 2.8 arcsec. Here we compare the output kinematic cubes to the kinematics fit with pPXF, where the average pixel fit χ^2/DOF = 2.44. The final column shows histogram of the relative residuals between the “velocity” and “spectral” kinematic maps, with the v_{LOS} and σ_{LOS} given with respect to the velocity resolution of the telescope.

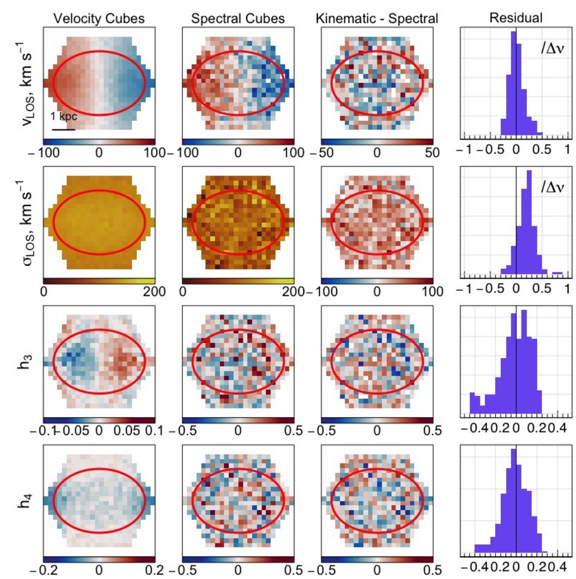

Figure 28. Case Study 4: The disk model built with BC03 templates observed with an intrinsic telescope resolution of $\lambda_{\rm LSF}^{telescope}$ = 4.56 Å at a low redshift distance of z = 0.0144. We convolve each plane in this cube with a Gaussian kernel with FWHM of 1 arcsec. Here we compare the output kinematic cubes to the kinematics fit with pPXF, where the average pixel fit χ^2/DOF = 209.06. The final column shows histogram of the relative residuals between the “velocity” and “spectral” kinematic maps, with the v_{LOS} and σ_{LOS} given with respect to the velocity resolution of the telescope.